Supporting Information for

# 3D-Printable Elastomers for Real-time Autonomous Self-healing in Soft Devices

Joseph G. Beckett[a,b,†], Carl J. Thrasher[c,*], Joshua Michonski[a,b], Robert M. Drexler[a,b], Sachin Babu[b,d], Allyson M. Cox[e], Braeden J. Windham[e], Zhenning Yu[b,d], Anesia D. Auguste[d], Abhiskek Shetty[f], Timothy H. Osborn[e], Robert L. Lowe[a,*], Laura A. Sowards[d], and Christopher A. Crouse[d,*]

[a] Department of Mechanical and Aerospace Engineering, University of Dayton, Dayton, OH 45469, USA

[b] UES Inc., Dayton, OH 45432, USA

[c] Department of Materials Science and Engineering, Massachusetts Institute of Technology, Cambridge, MA 02142, USA

[d] Air Force Research Laboratory, Materials and Manufacturing Directorate, Wright-Patterson AFB, OH 45433, USA

[e] Additive Manufacturing Technology Development, University of Dayton Research Institute, Dayton, OH 45469, USA

[f] Anton Paar USA, Inc., Ashland, VA 23005, USA

[*] Corresponding authors: cthrash@mit.edu | robert.lowe@udayton.edu | christopher.crouse.1@us.af.mil

[†] Present address: Department of Mechanical Engineering, University of Michigan, Ann Arbor, MI 48109, USA

**Methods and Materials:**

*Materials:* All chemicals were purchased from Sigma-Aldrich (USA) and used as received, unless otherwise noted. The components of the resin were 2-hydroxyethyl acrylate (HEA; 292818), pentaerythritol tetrakis(3-mercaptopropionate) (PETMP; 381462), 1,6-hexanediol diacrylate (HDDA; 246816), and phenylbis(2,4,6-trimethylbenzoyl)phosphine oxide (BAPO; 511447). Green food dye used in the print-compatible resin was purchased from the Kroger Company. The dye is an aqueous mixture of Yellow-5 and Blue-1 with propylene glycol and propylparaben. The compositions of the resin components are tabulated in Table S1.

*Resin synthesis and storage:* After all liquid components were combined, the resin was vortex mixed for 1 min to create a homogeneous solution (Note S4). BAPO was then combined with the liquid components (Note S5). A second 1 min cycle on the vortex mixer was used to ensure that the initiator was entirely dissolved into the resin. All resin for this work was cured shortly after mixing (no more than 24 hr for cast samples and 48 hr for printed samples).

*Resin rheology:* Dynamic mechanical analysis was conducted on a TA Instruments Discovery HR-3 rheometer using 40-mm steel parallel plates. Frequency sweeps were conducted at 25 °C from 1/s to 100/s on resin produced without green dye (Fig. S22). Three separate sweeps were conducted to verify repeatability.

*Casting:* Cast samples were cured with an LED power supply (CF2000, Clearstone) equipped with a 365-nm bulb (JL1 Series 365E-48). The power supply's UV unit was positioned 25 cm above the top of the mold and set to 25% power. A power meter (UP19K-15S-H5-DO, Gentec-EO) measured a peak flux of 2.9 mW/cm$^2$ at a wavelength of 365 nm directly under the UV source. Polymerization involved a continuous cure of 4 min unless otherwise noted (Table S2 and Fig. S19). Studies of the curing duration (Fig. S20-21) indicated that curing was effectively complete between 60 and 120 s. Prior to curing, 5.8 mL of resin was transferred via micropipette to each specimen channel. Samples were cured in various PDMS and Mold Max (Smooth-On, Inc.) molds.

*3D printing:* A stock 3D Systems Figure 4 Modular DLP printer with no physical alterations was used for 3D printing (Note S6). A 50-$\mu$m layer thickness was used in the prints with an 11.27 s cure time for each layer. The UV sources provided a UV flux of 19.07 mW/m$^2$ at a peak wavelength of 408 nm as measured using a digital spectrometer (BLACK-Comet, StellarNet, Inc.). Green food dye used in the resin served the sole purpose of preventing overpenetration of the UV light during the polymerization reaction. 4 $\mu$m of height compensation in the $z$-direction was used to account for deformation of the low-modulus prints under their own weight. Rapid resin refresh between layers and excellent heat dispersion is encouraged by the low viscosity of the resin, measured to be approximately 0.007 Pa-s (Fig. S22). Tensile specimens were printed in an orientation such that the joined faces of adhered layers were orthogonal to the uniaxial loading (Fig. S23). Thus, tension results seek the properties of the bulk printed material rather than interlayer adhesion. Between each layer, the build tray moved upwards and then lowered back down over 0.5 s to the appropriate height for the next layer. A 0.1-s pause was implemented before the part was lowered to its printing height between layers. 0.28-mm-wide pillars were used as external supports on the bottom of all prints with the

exception of the gyroid lattice and tension specimens, which were printed directly onto the build tray with no supports. No internal supports were used when printing the pneumatic actuators. All printed parts were cleaned using 99% IPA. Some soft actuator prints were also cleaned in an ultrasonic IPA bath to aid in resin removal from the bellows. A 5-min post-cure (300-550 nm) in a UV print box (LC-3DPrint Box, NextDent) was applied to all DLP-printed parts (Note S7).

*Sample storage:* After curing, all cast and printed samples were stored for 1 week under one of two humidity conditions at ambient temperature. "Dehydrated" samples were stored in a nitrogen-purged desiccator at approximately 15% RH. "Ambient" samples were stored in a UV-protected box at an ambient humidity of approximately $45 \pm 20\%$ RH. All samples were stored on PTFE-coated coarse mesh to prevent sticking and promote air flow during storage.

*Mechanical characterization:* Quasi-static uniaxial tension testing was conducted on an Instron 3365 extended-height load frame with a 2-kN Instron load cell for force measurement. Strain measurements were provided by an Instron long-travel clip-on extensometer. All tensile specimens adhered to ASTM D412 type C specimen dimensions. Cast specimens were molded to shape, while DLP-printed specimens were cut from 3-mm-thick printed sheets using a steel die and an arbor press. Measurements of specimen gauge sections were taken using both direct measurements (digital caliper) and optical measurements (FLIR BFS-U3-88S6M-C camera and ImageJ). Three measurements were taken along different parts of the gauge, averaged, and used in subsequent calculations of engineering stress. Unless otherwise stated, all uniaxial tensile tests were conducted at 500 mm/min, following the ASTM D412 test standard. The samples had 15 mm of material gripped on either end, yielding a distance between the grips of 85 mm and a nominal strain rate of approximately 0.1/s. Cyclic tension tests were conducted over the course of five displacement-controlled cycles between crosshead displacements of 0 and 190 mm. In the cyclic tests, engineering strain was calculated by dividing crosshead displacement (measured by the built-in Instron linear variable differential transformer (LVDT)) by the grip-to-grip distance of 85 mm.

To conduct self-healing tests, tension specimens were cut using a clean razor blade. Samples were allowed to rest for 5 min prior to realignment by hand. After manual realignment, the specimens were allowed to sit for another 5 min before they were tested in the load frame. All DIC images were taken using a machine vision camera (BFS-U3-88S6M-C, FLIR) with a 35-mm focal length lens (HP series, Edmund Optics). Cross polarization was used to reduce spectral reflections on the surface of the material. India ink (Super Black, Speedball) was applied to the surface of the specimen using an airbrush. Two Genaray Spectro LED 500IIB panels were used to provide sufficient lighting for the images. All images were acquired using an acquisition rate of 25 Hz with an exposure time of 15 ms and an aperture of f/4.0. All post-processing was conducted using commercial DIC software (VIC-2D, Correlated Solutions). The DIC analyses were conducted using an incremental formulation with a subset size of 11 px, step size of 1 px, and strain filter size of 15 px. The scale of the images is approximately 12 px/mm. Default low-pass image filtering was performed using 6-tap interpolation.

*Elastomer rheology and modified probe tack test:* All rheological testing was conducted on 2-mm-thick/25-mm-diameter cast discs of dehydrated material. Humidity and temperature sweeps were performed using an Anton Paar MCR 702 MultiDrive with 25 mm parallel plates (L-PP25/TD/TS) with a

CTD180 HR convection oven and an MHG 100 humidity generator. Sinusoidal torsion (displacement amplitude of 10 $\mu$rad and frequency of 1 Hz) was applied to the specimens by the plates. A 10 $\mu$rad amplitude was selected because the material's response falls within the linear viscoelastic region, based on pre-test amplitude sweeps (Figure S24). Samples were placed under 1 N of compressive force prior to the start of oscillatory deflections. The temperature sweep was conducted at a rate of 1 °C/min from 5 to 70 °C at 20% RH. For the humidity sweeps, the samples were conditioned at 25 °C at 10% RH for 100 min prior to testing. For the continuous humidity sweep, the humidity was increased at a rate of 0.05% RH/min. The stepped test increased the humidity rapidly in increments of 10% RH when a change of less than 0.1% in complex shear modulus was detected over the average of the last fifteen measured data points. For repeated self-healing tests (using a modified probe tack test), a TA Instruments RSA-G2 solids analyzer with 25 mm steel parallel plates was used. For each cycle, the samples were compressed to 2.1 N, allowed to rest for 1 s, and rapidly separated at a rate of 10 mm/min. Each sample underwent five compressive cycles.

*Pneumatic actuator preparation and healing:* A generic pneumatic actuator was designed with a square gasket at one end (Figure S18). A custom gasket plate was fabricated to provide the interface between the pressure-regulated compressed shop air and the soft robot. All actuators were coated on their exterior with a thin layer of PTFE dry lubricant spray (Anti-Seize Technology) to minimize unwanted adhesion. During application, the spray can was held approximately 1 ft from the surface of the post-cured actuators. Light coats of the spray were carefully applied to all external surfaces of the prints. Per the manufacturer's instructions, the spray was allowed to dry for at least 5 min before the actuators were handled. The applied PTFE was shown to have no significant effect on the water content equilibrium of samples (Note S8).

*Statistical analysis and plotting*: All statistical analyses were performed using `Matlab` (v. 2024a, MathWorks, USA). All data were reported as the mean $\pm$ sample standard deviation, with a minimum sample size $n = 3$ (Fig. S8 and Table S2). During plotting, small moving means were carefully used in several plots (i.e., Figs.2d-e, S11-14, and S21) to help eliminate excessive random noise from the data and improve readability.

**Supporting Note S1 (Soxhlet extraction):** A cured specimen (irradiated for 240 s at 365 nm) was placed into a glass fritted extraction thimble, transferred to a Soxhlet extraction apparatus, and subjected to refluxing methanol for a total of 72 hr. After extraction and subsequent drying in a vacuum oven, the recovered mass of the dogbone was approx. 64% of the original mass. The eluent was then transferred to a rotary evaporator to remove the methanol. The mass of the dissolved residue, after drying in a vacuum oven, was 36% of the original mass, matching the mass lost from the dogbone. This data suggests that approximately one-third of the hydrogel mass exists as low-molecular weight oligomer that is not directly bound to the cross-linked network.

**Supporting Note S2 (Water content estimation):** In order to determine water content, the mass evolution study in Fig. S6 and the TGA data of desiccator stored and freshly synthesized material in Fig. S21 were examined. The mass evolution study comparing the weight change of ambient and desiccator stored materials as they equilibrate shows about 1.5% weight difference after 2 weeks due to differences in water content ($\sim$0.8% mass gain during ambient storage, $\sim$0.7% mass loss during desiccator storage). This can be taken as a lower bound of water content for ambiently stored materials, but is likely an underestimate as it does not account for the water content of the desiccator material. Alternatively, TGA data of freshly synthesized material can be examined to find the mass loss at 200 °C, which we find as about 3.7% mass loss on average. This, when added to the $\sim$0.8% mass gain from storage (for 4.5% total), represents an upper bound for the water content of ambiently stored materials. However, this is likely an overestimate as it will include mass loss from unreacted monomer (HEA monomer has a boiling point around 200 °C), which is expected as conversion approaches, but does not fully reach 100%. So, with high confidence, the water content in ambiently stored materials can be expected to fall between 1.5-4.5% by weight. For a best guess estimate, we examine the mass loss from TGA data at 120 °C, which should largely reflect mass loss from absorbed water. We find that freshly synthesized materials have a mass loss of 1.9% at 120 °C, while desiccator stored materials have a mass loss of 1.1% at 120 °C. The 0.8% difference between these values is consistent with the $\sim$0.7% difference reported in the mass evolution study between freshly synthesized and desiccator stored materials. Finally, adding the expected mass gain from ambient storage to the freshly synthesized mass loss, a best guess estimate of 2.7% water content was determined for ambiently stored materials.

**Supporting Note S3 (Autonomous Self-healing of Actuator):** As the actuator inflated and approached its maximum bending angle, pressure was released. Once the actuator relaxed to its nearly undeformed state, an X-Acto knife was forced into its flat end, opposite the bellows. The resulting gash was approximately 7 mm long. The knife was removed from the actuator after several seconds. Care was taken to allow the device to autonomously realign the damaged regions when the knife was removed by not holding the robot adjacent to the cut when the knife was extracted. Immediately after the knife was removed, the same 1.5 psi of pneumatic pressure was released back into the actuator. Sound was recorded to verify that no air was escaping the actuator through the healed interface.

**Supporting Note S4 (Precursor Mixing):** All precursors were mixed in large glass vials coated in aluminum foil to minimize light exposure. HEA (95.75 wt%) was weighed out on various scales with a minimum resolution of 0.1 g. The 0.1 g readability balance was only used when mixing resin in batches greater than 40 g, which exceeded the maximum capacity of the other available scales. PETMP (3 wt%) and HDDA (1.25 wt%) were weighed out on an analytical balance (AE100, Mettler Toledo) with a readability of 0.1 mg. When the total mass of the resin batch was less than 40 g, the HEA, PETMP, and HDDA were mixed in the same vial. When the total mass exceeded 40 g, the PETMP and HDDA were mixed in a

separate vial and subsequently combined with the HEA. Backwashing was important to ensure complete transfer, especially since PETMP is quite viscous. For the DLP print-compatible resin, green food dye (0.5 wt% on top of the base resin at 100 wt%) was added to the resin.

**Supporting Note S5 (Initiator Ratio):** A surplus of initiator was used in the resin to overwhelm the monomethyl ether hydroquinone inhibitor in the HEA monomer, as is common in many commercial-scale resin chemistries.

**Supporting Note S6 (DLP Vat):** The DLP printer uses an oxygen-permeable bottom film to prevent mechanical adhesion to the vat, which has been found to facilitate the printing of low-modulus elastomers with minimal defects.

**Supporting Note S7 (Post-curing):** To repeatably store the adhesive hydrogel, cured parts were stored on a polytetrafluoroethylene (PTFE) coated coarse grilling mesh to prevent them from sticking to the bottom of the post-cure box. In the early stages of the project, DLP-printed tensile specimens were cured using all of the bulbs in the post-cure box. For the proof-of-concept prints, only 2 of the 12 UV bulbs on the lid were used to minimize heating within the enclosure. The internal walls of the post-cure box are reflective to promote even exposure of all surfaces to UV light.

**Supporting Note S8 (Storage of PTFE-coated specimens):** We performed a study to monitor the hydration of cast and printed specimens with and without a PTFE coating applied. The standardized procedure reported in the Experimental Methods was used to apply the coating. The specimens were weighed and then dried under vacuum at 80°C for 16 hr to remove absorbed water. The samples were then placed in an elevated humidity environment (76% RH) at 22°C for 72 hr, after which they were weighed to compare moisture uptake. For the printed material, the samples with and without the PTFE coating experienced a weight gain of 14.31% and 14.88%, respectively. Similarly, for the cast material, the weight gain was 14.85% and 14.51%, respectively, for the coated and uncoated specimens. Thus, we can conclude that even if the PTFE spray coating does slow moisture uptake, it does not have a signficant enough impact on moisture equilibration rates to be of concern given the long equilibration times used throughout this work.

**Supporting Table S1:** Tabulated resin formulation data.

Two main resin compositions were used throughout this work. The only difference between the formulations was the presence of green food dye in the DLP-printed version of the resin.

| Component | wt% (base,dyed) | mol% (base,dyed) |
|---|---|---|
| 2-Hydroxyethyl acrylate | 95.63, 95.16 | 98.57, 95.40 |
| Pentraerythritol tetrakis(3-mercaptopropionate) | 3, 2.98 | 0.734, 0.710 |
| Hexanediol diacrylate | 1.25, 1.24 | 0.660, 0.639 |
| Phenylbis(2,4,6-trimethylbenzoyl)phosphine oxide | 0.125, 0.124 | 0.0357, 0.0346 |
| Green food dye | 0, 0.497 | 0, 3.21 |

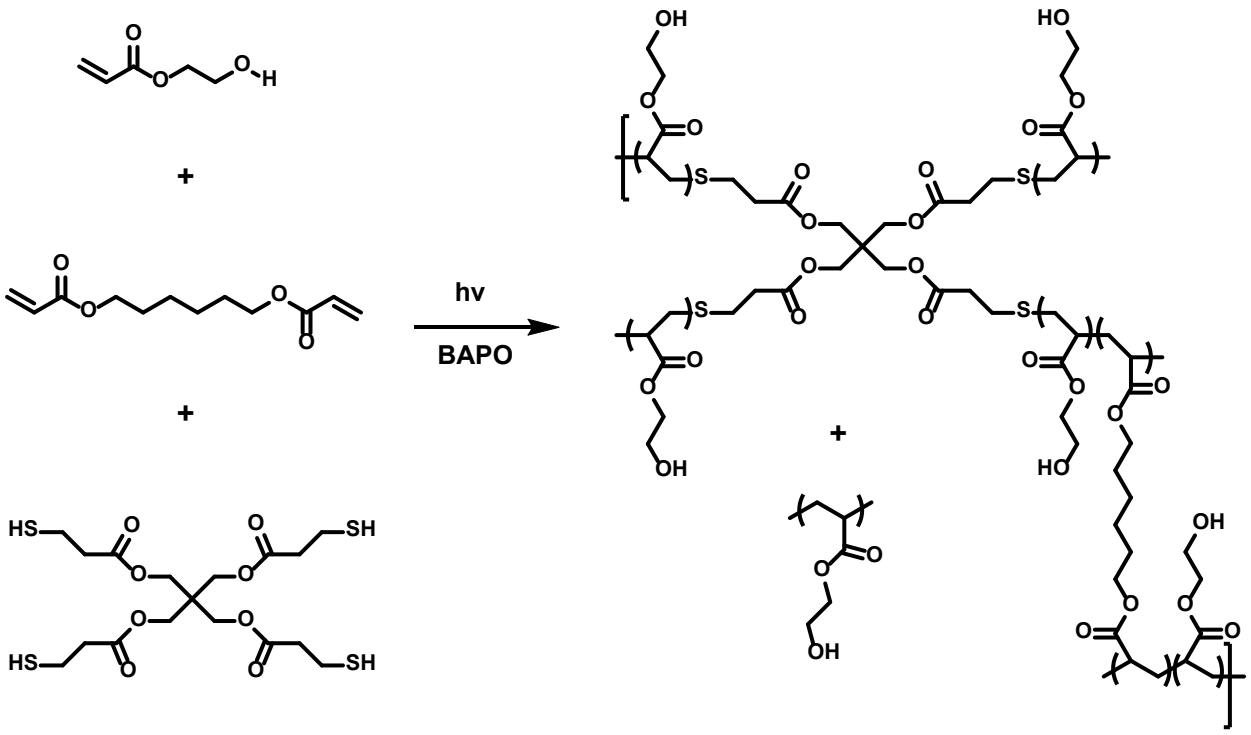


**Supporting Scheme S1:** Formation of example polymer network and oligomeric polymer chain structures.

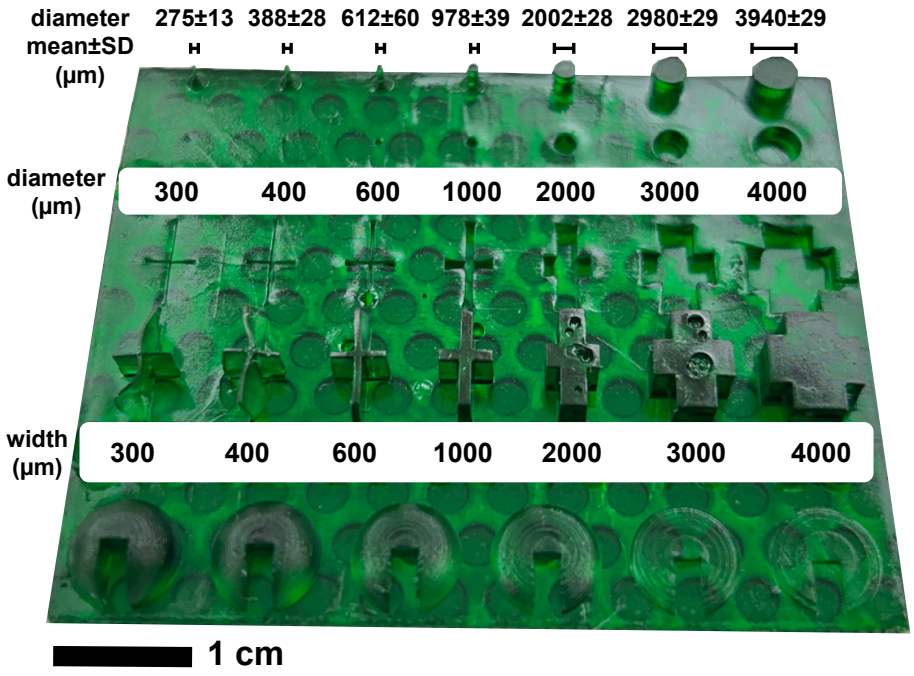


**Supporting Figure S1:** DLP print resolution and dimensional accuracy test.

A dedicated test specimen comprising features (crosses and pillars) extruded from and cut into a body of sizes ranging in diameter/width from 4 to 0.3 mm was printed. The print demonstrated slight undercuring and few defects (primarily a few bubbles that nucleated towards the end of the print). Notably, several of the smallest crosses buckled under their own weight once the completed build plate was inverted, thus casting doubt on the utility of printing finer features in most practical applications. To quantify dimensional accuracy, caliper measurements were collected on the extruded pillars, revealing nearly a 98.5% and 91.7% dimensional accuracy, respectively, for the 4 and 0.3 mm pillars. The measurements and standard deviations are reported for all of the pillars in the figure.

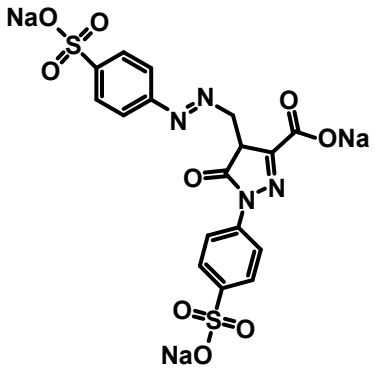


Yellow 5

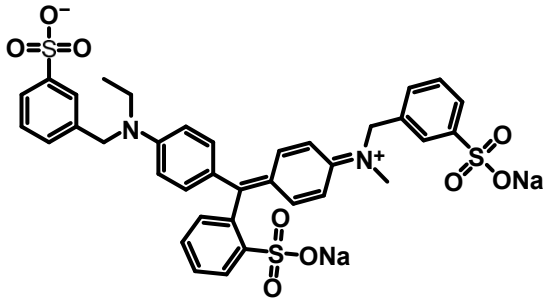


Blue 1

**Supporting Scheme S2:** Structures of dyes in the green food coloring used in the DLP resin.

These dyes do not contribute to the photopolymerization chemistry. They are arbitrary and can be replaced by any suitable light-absorbing dye or pigment.

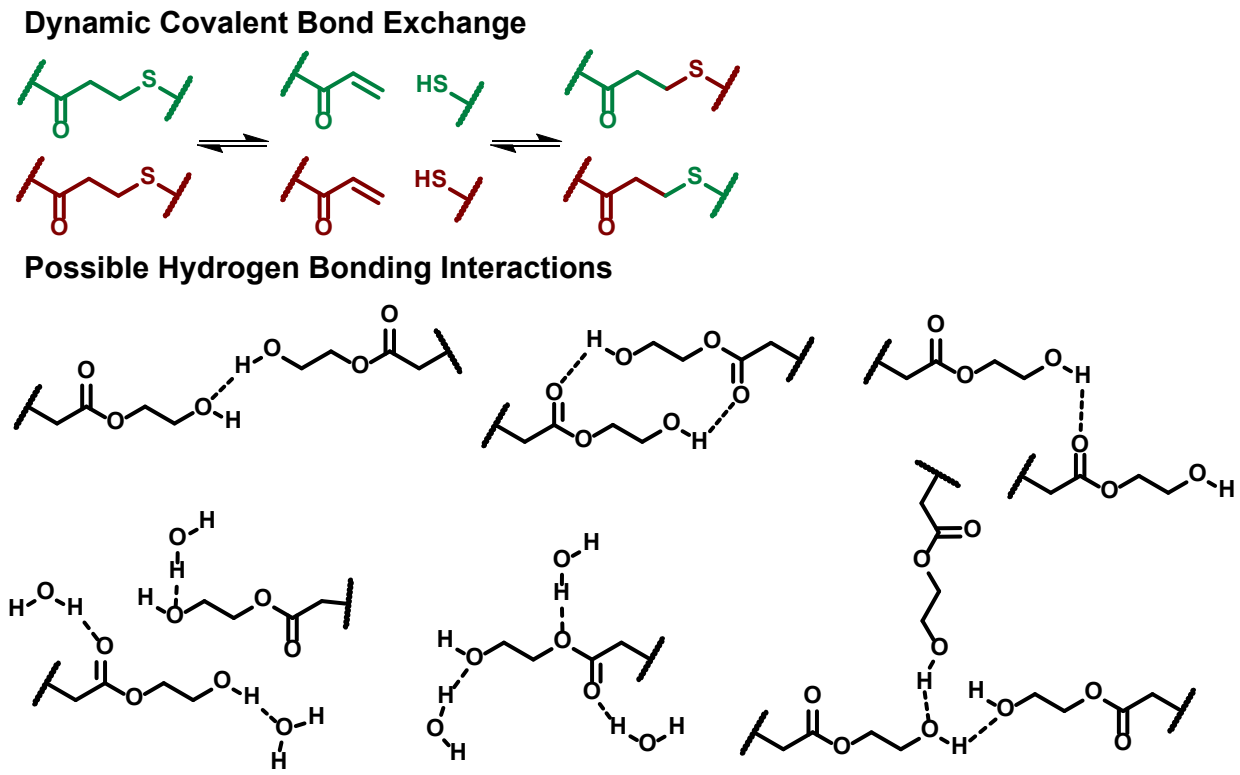


**Supporting Scheme S3:** Dynamic bond exchange mechanism and hydrogen bonding modes for poly(2-hydroxyethyl acrylate) with and without water.

The dynamic exchange of thioether moieties in this material is only expected to occur at high temperatures[56], and tensile results depicted in Figure S3 suggest that even after extended time at elevated temperature, these interactions only minimally contribute to total self-healing. Instead, self-healing tends to be dominated by hydrogen bonding interactions. These interactions are highly dynamic, allowing for rapid healing at room temperature. However, the hydrogen bonding capacity of these materials is moisture sensitive, as the water molecules can compete for hydrogen bonding sites. In this sense, water acts as a plasticizing agent in the material.

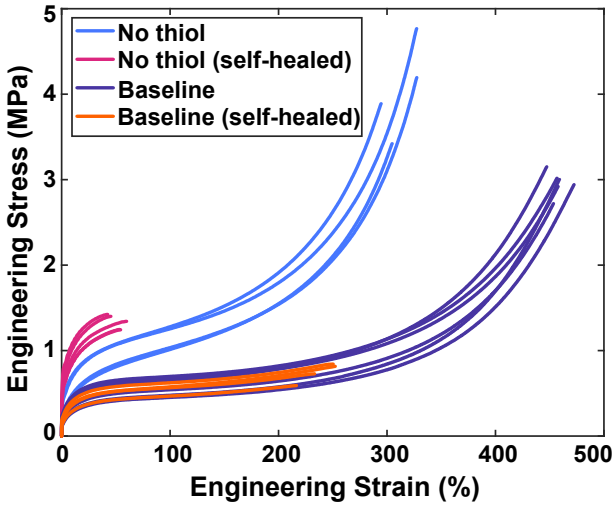


**Supporting Figure S2:** Cast samples with and without the thiol component of the resin tested under uniaxial tension.

To confirm the importance of the 4-arm thiol for achieving the material's self-healing efficiency, a batch of resin was formulated without the thiol component. All other molar ratios were left unchanged. The resulting tensile data for the thiol-free material revealed a significantly stiffer material that exhibited a higher ultimate tensile strength and a decreased strain at fracture. The thiol-free material was notably less tacky, translating to significantly reduced self-healing performance (59% reduction in toughness post-healing relative to its thiol-containing counterpart).

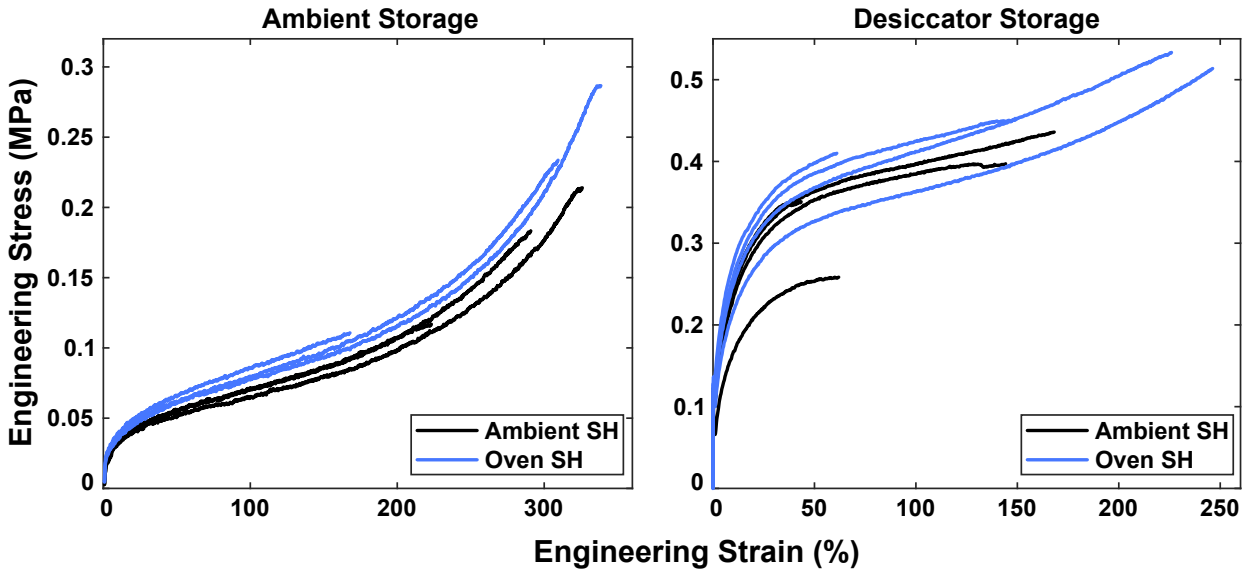


**Supporting Figure S3:** Investigation of self-healing (SH) mechanism in ambient and dehydrated samples tested under uniaxial tension.

This set of experiments was performed to verify that the material did not exhibit significant self-healing capacity due to thermally-activated dynamic covalent bonding. After casting, all samples were stored for 1 week at their respective storage humidity. Subsequently, all samples were fractured across their geometric center using a razor blade and re-aligned manually. Healed samples were immediately transported to a 90 °C oven for 24 hr, then stored for another 1 week period in their specified environment prior to testing. Ambient samples were allowed to rest for another week post-healing to mimic the extended timeline of the oven samples. The differences in stress-strain response between the ambient and oven self-healed samples are relatively small, suggesting minimal, if any, dynamic covalent bonding. In light of time-temperature equivalence for polymer degradation, this test also suggests that prolonged storage of the cured material has only a small effect on its stress-strain response.

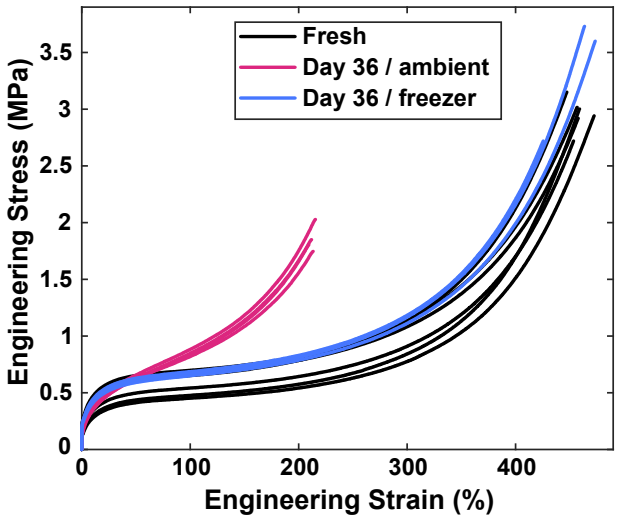


**Supporting Figure S4:** Uniaxial tension results for cast samples produced from fresh resin, resin stored at ambient temperature, and resin stored at -20 °C.

The acrylate and thiol components of the resin are susceptible to reacting with one another under ambient conditions. To quantify the stability of the chemistry, resin was stored for 36 days in a dark drawer at ambient temperature. Another vial of the same batch of resin was stored in a freezer at -20 °C. As expected, the ambient-stored resin showed significantly different mechanical properties than specimens cast with fresh resin. A reaction between the thiol and acrylate components at ambient temperatures is the predicted source of this degradation. It is worth noting that the tackiness of the material was also significantly reduced, which suggests that the hydrogen bonding in the material was also affected by the thiol-acrylate reaction. Resin storage at -20 °C seems to have eliminated the reaction by dropping the thermal energy of the system sufficiently low enough to prevent the reaction from meaningfully taking place. The results suggest that long-term storage of the mixed resin is feasible when stored at or below -20 °C without hindering the performance of the resin.


**Supporting Figure S5:** 3D "Benchy" printed on a 3D Systems Figure 4 Modular DLP printer.

This print demonstrates the ability of the resin to print overhangs with minimal supports. The original creator of this well-known benchmark print is Creative Tools.

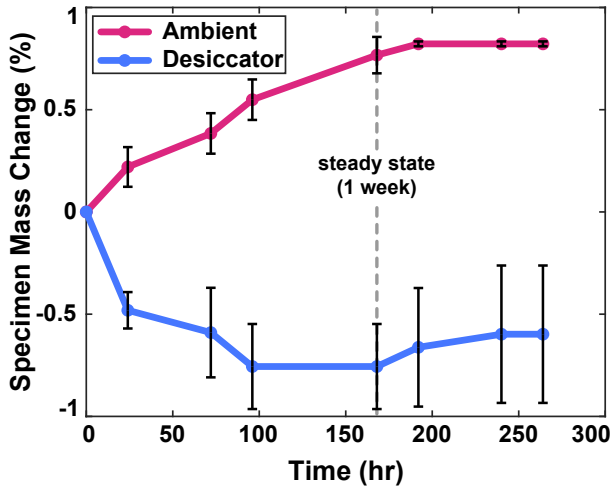


**Supporting Figure S6:** Mass evolution study to monitor water content of cast material during sample storage.

To help establish a rough duration of storage needed to reach a repeatable steady state water content, samples were weighed periodically during storage. Samples stored in ambient (45 $\pm$ 20% RH) and desiccated (15% RH) conditions were studied. After approximately one week, all specimens studied were sufficiently near steady state. This finding was used to inform the one-week storage periods for specimens prior to testing. In our experience, this duration is sufficient for achieving repeatable results.

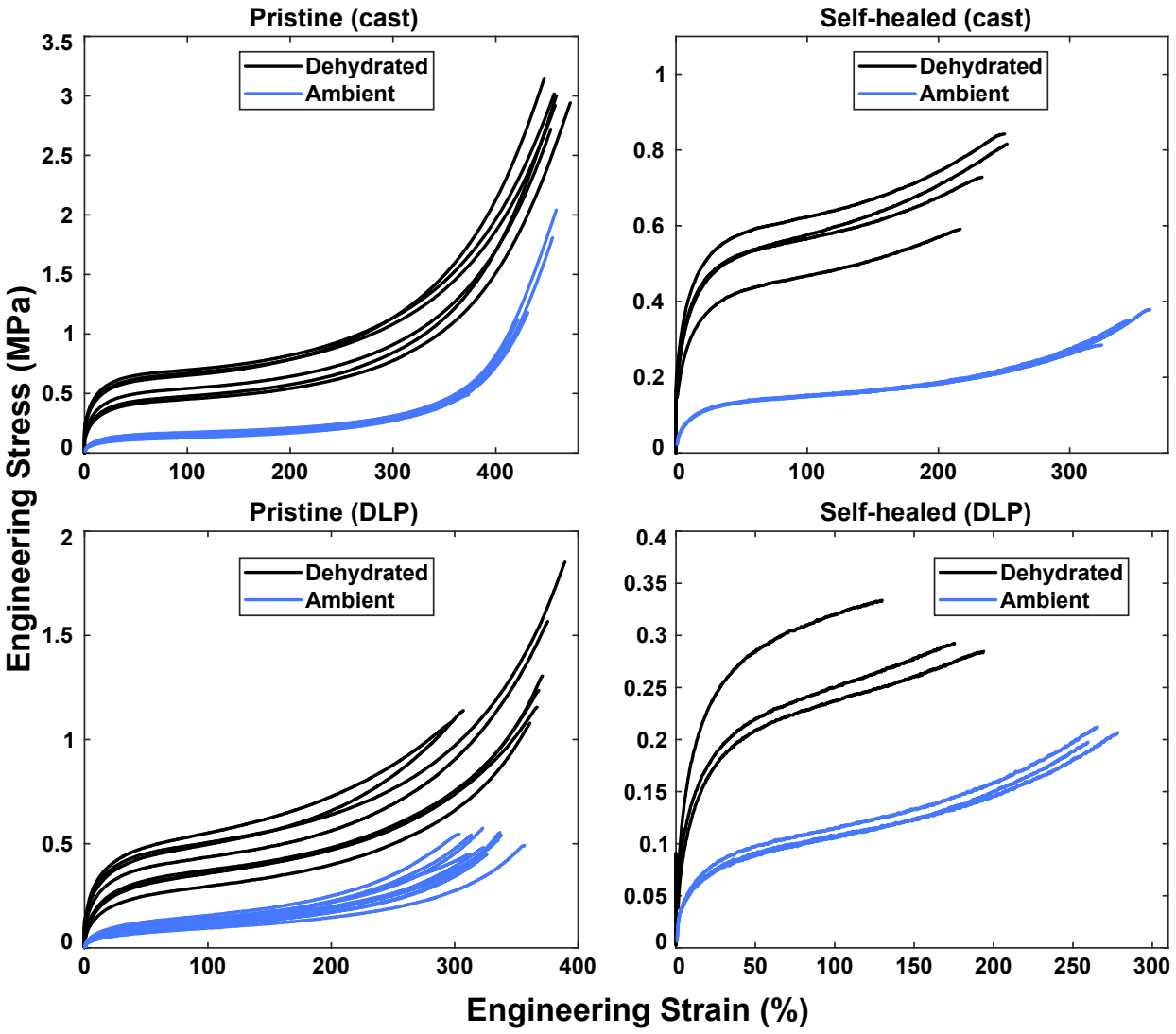


**Supporting Figure S7:** Baseline tension test data showing property variation with water content (ambient/dehydrated), curing technique (cast/DLP), and damage (pristine/SH).

Some samples were comprised of specimens made in different batches. As a result, some specimens within the same sample were stored in slightly different humidity contents. Generally speaking, repeatability within samples from the same batch was noticeably better than between different batches. In cast samples, the dehydrated material was 113% tougher than its hydrated counterpart after self-healing. Dehydrated DLP printed samples were only 21% more tough than their ambiently stored counterparts.

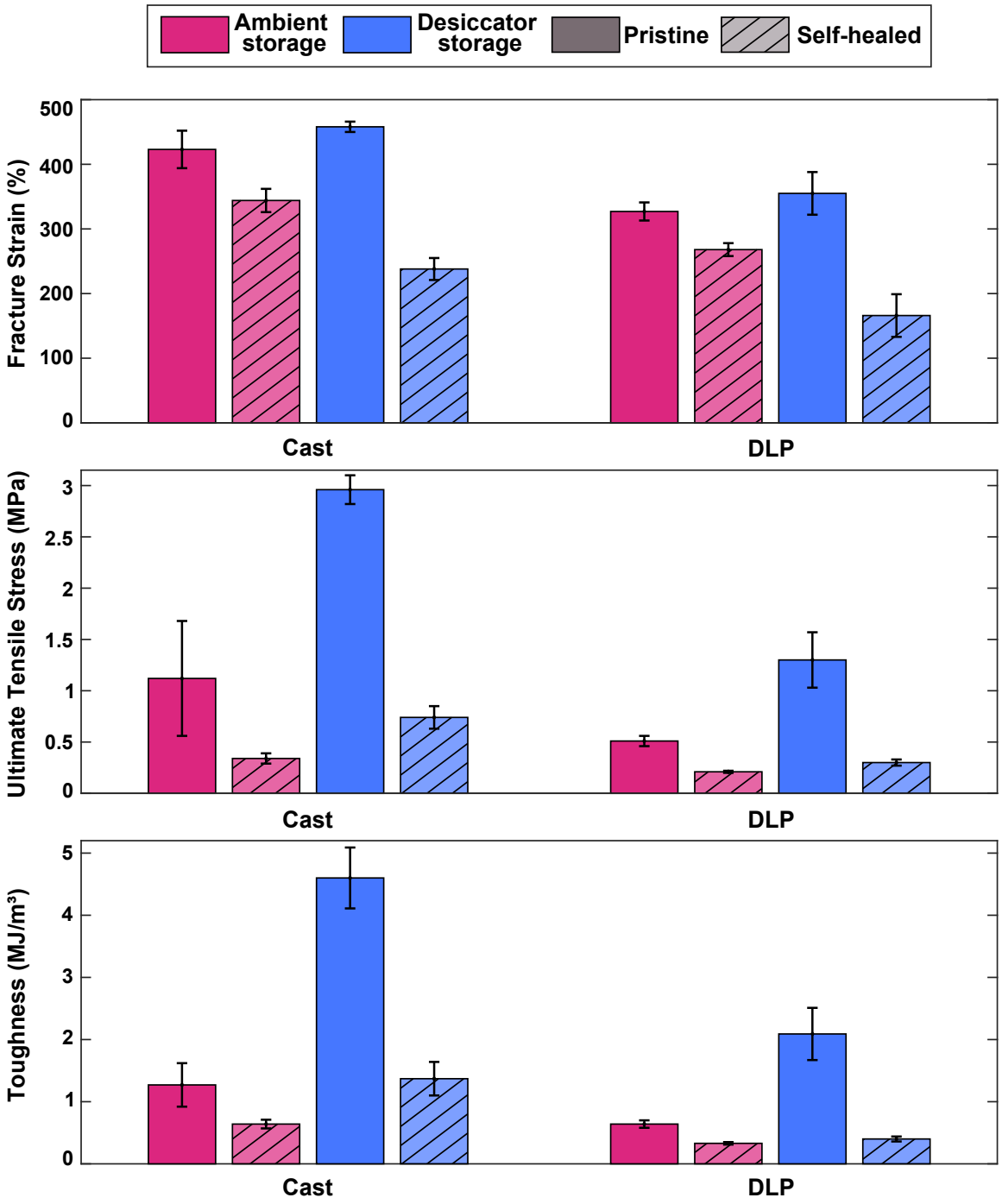


**Supporting Figure S8:** Baseline statistics comparing property variation with water content (ambient/dehydrated), curing technique (cast/DLP), and damage (pristine/SH).

**Supporting Table S2:** Tabulated statistics on mechanical testing data from uniaxial tension experiments.

All values are reported with the format of mean ± standard deviation (sample). Fracture strain is reported in engineering strain, and ultimate tensile strength is reported in engineering stress. Engineering stress-strain was used in favor of true stress-strain for consistency with other reported mechanical property data in the self-healing elastomer literature. Samples in the elevated temperature self-healing study are not reported in this table because those samples used different protocols for self-healing, curing, etc. before the methods for handling and healing were optimized for repeatability and performance.

| Sample parameters | Sample size | Fracture strain (%) | Ultimate tensile stress (MPa) | Toughness ($MJ/m^3$) |
|---|---|---|---|---|
| cast/amb. stor. | 7 | 423±29 | 1.12±0.56 | 1.27±0.35 |
| cast/desic. stor. | 6 | 458±8 | 2.96±0.14 | 4.60±0.49 |
| DLP/amb. stor. | 12 | 327±14 | 0.51±0.05 | 0.64±0.06 |
| DLP/desic. stor. | 8 | 355±33 | 1.30±0.27 | 2.09±0.42 |
| cast/amb. stor./SH | 3 | 344±18 | 0.34±0.05 | 0.64±0.07 |
| cast/desic. stor./SH | 4 | 238±17 | 0.74±0.11 | 1.37±0.27 |
| DLP/amb. stor./SH | 3 | 268±10 | 0.21±0.01 | 0.33±0.02 |
| DLP/desic. stor./SH | 3 | 166±33 | 0.30±0.03 | 0.40±0.04 |
| cast/flat graft/desic. stor./SH | 4 | 40±12 | 0.28±0.02 | 0.09±0.04 |
| cast/35° graft/desic. stor./SH | 3 | 176±107 | 0.44±0.10 | 0.65±0.48 |
| cast/17.5° graft/desic. stor./SH | 4 | 334±26 | 0.84±0.13 | 1.74±0.25 |
| cast/amb. aged resin/ desic. stor. | 4 | 213±3 | 1.86±0.12 | 2.00±0.10 |
| cast/-20°C aged resin/ desic. stor. | 3 | 454±25 | 3.35±0.55 | 5.28±0.64 |
| slow cast/desic. stor. | 4 | 502±22 | 2.26±0.21 | 3.97±0.47 |
| slow cast/desic. stor./SH | 6 | 221±53 | 0.78±0.08 | 1.45±0.40 |
| slow cast/resin with water/desic. stor. | 5 | 517±19 | 2.53±0.38 | 4.07±0.49 |
| slow cast/resin with water/desic. stor./SH | 6 | 253±30 | 0.65±0.03 | 1.30±0.16 |
| slow cast/no thiol resin/desic. stor. | 4 | 314±17 | 4.07±0.56 | 5.18±0.70 |
| slow cast/no thiol resin/desic. stor./SH | 5 | 51±7 | 1.33±0.08 | 0.57±0.06 |

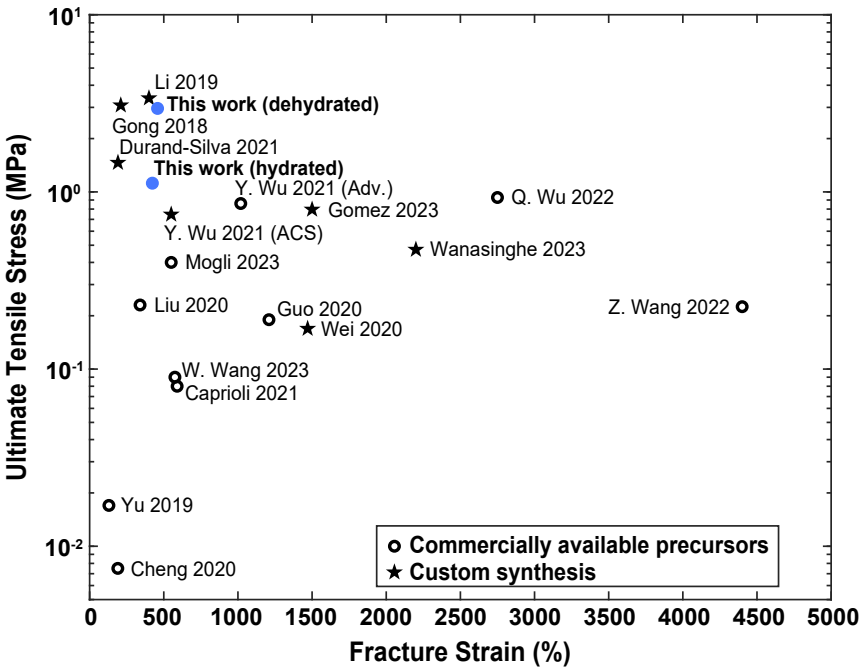


**Supporting Figure S9:** Ashby diagram (UTS vs. fracture strain) of known intrinsically self-healing photocurable self-healing elastomers in their pristine state.

For the literature review, engineering stresses and strains at fracture were recorded for the best (generally the toughest) material properties reported in each work. All self-healing photocurable elastomers that the team was aware of prior to manuscript submission were reported. The ultimate tensile strength of our material in its dehydrated state is nearly identical to the results of Gong et al. in 2018 and Li et al. in 2019, both of which use custom-synthesized precursors.

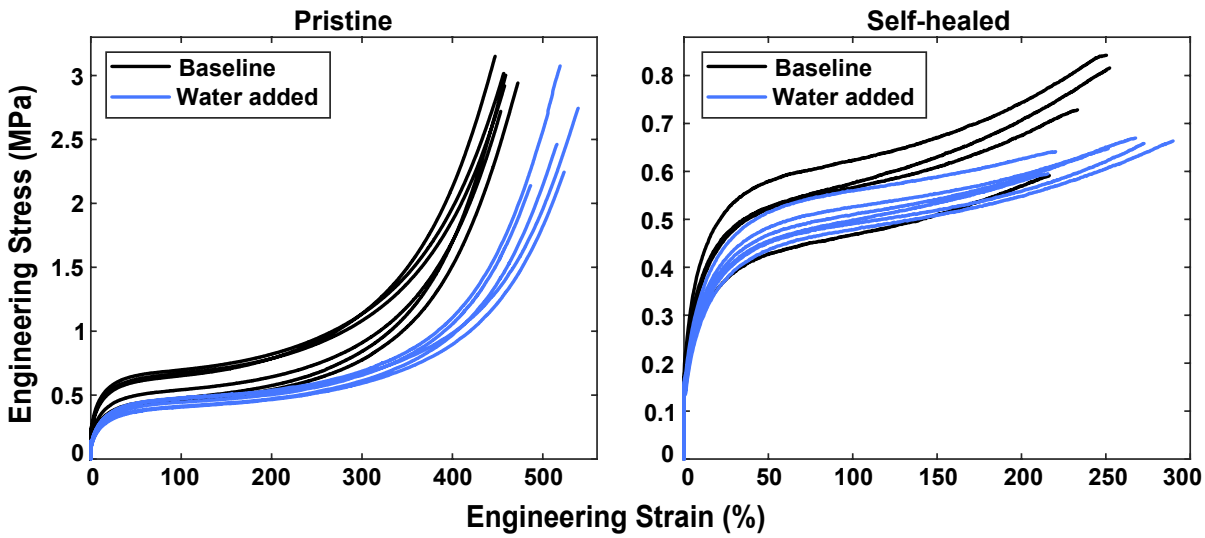


**Supporting Figure S10:** Samples cast from resin with added water, tested in uniaxial tension.

To mimic the non-negligible amount of water added to the DLP-printed resin from the green food dye, water was added to dye-free resin. The samples were cast to isolate the effect of water on mechanical properties. All samples were stored in the nitrogen-purged desiccator for 1 week prior to testing. The tensile test results suggest that although a majority of the water is clearly removed during storage, the specimens were still less stiff than the baseline dehydrated cast samples. Healed samples performed similarly to their baseline counterparts, apart from a small decrease in modulus. This is presumably due to a slightly higher water content even after storage or some minor change in the polymerization due to the presence of additional water.

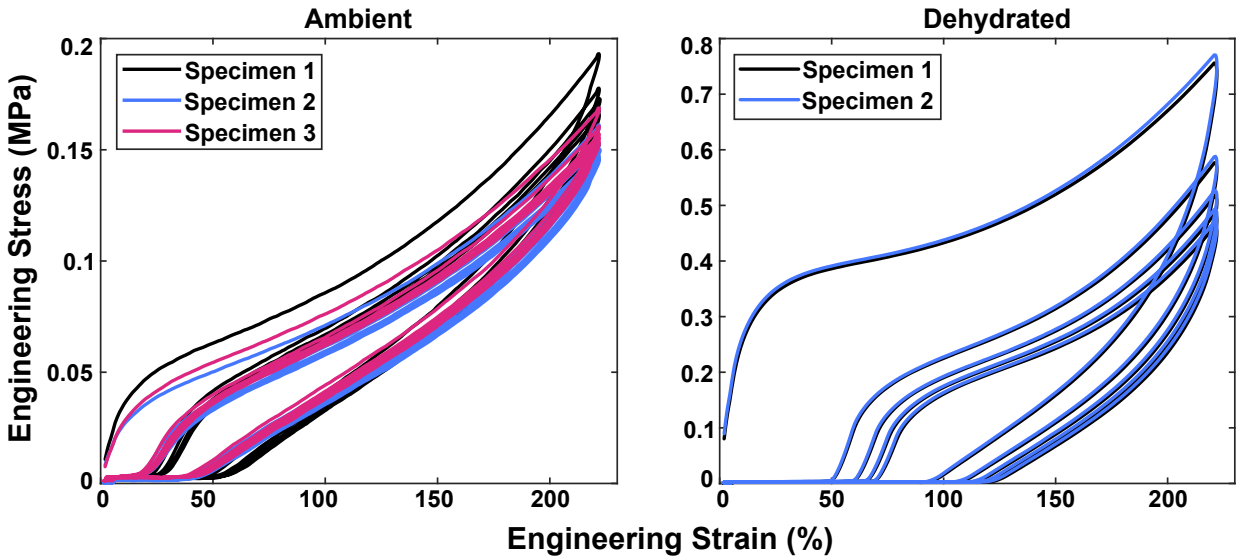


**Supporting Figure S11:** Displacement-controlled cyclic tension study on cast specimens.

When dehydrated, the material exhibits strain softening with every passing cycle. As expected, the water is able to swell the hydrogel network sufficiently to reduce viscoelastic effects even at moderate strain rates. Storing the material in ambient conditions allows for an almost complete elimination of the viscoelastic effects within the material after the first cycle.

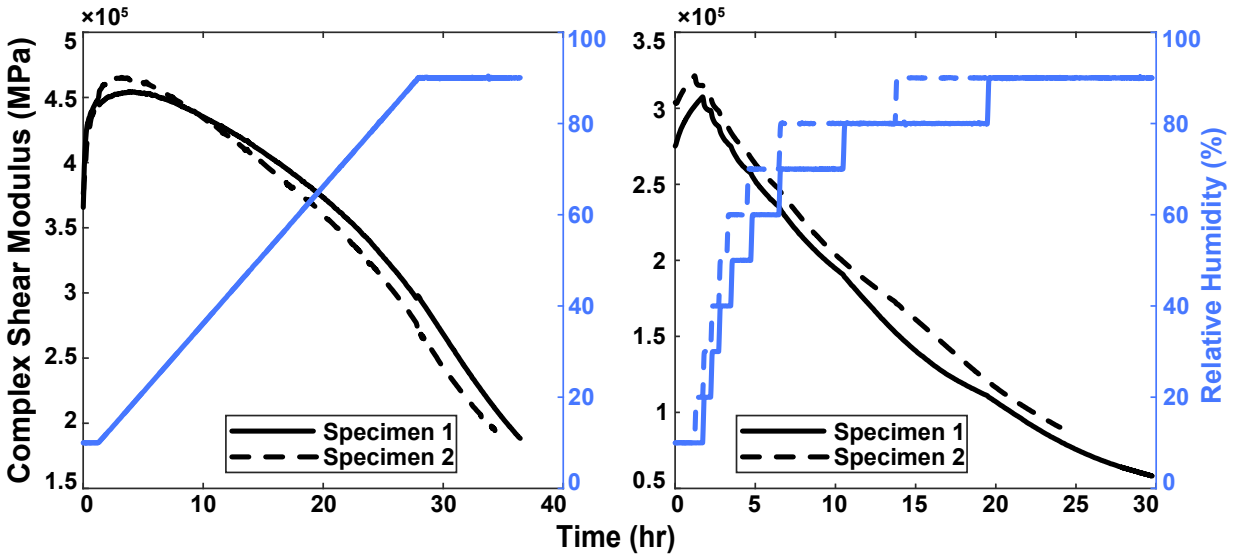


**Supporting Figure S12:** Long-duration rheological analysis of cast material performance as a function of relative humidity of the surrounding environment.

Dynamic mechanical analyses were used to showcase how the material's mechanical properties can be tuned by adjusting the relative humidity of its surrounding environment. Both continuous and stepped humidity sweeps were conducted using a precise humidity controlled environmental chamber while the disk-shaped specimens were loaded in torsion.

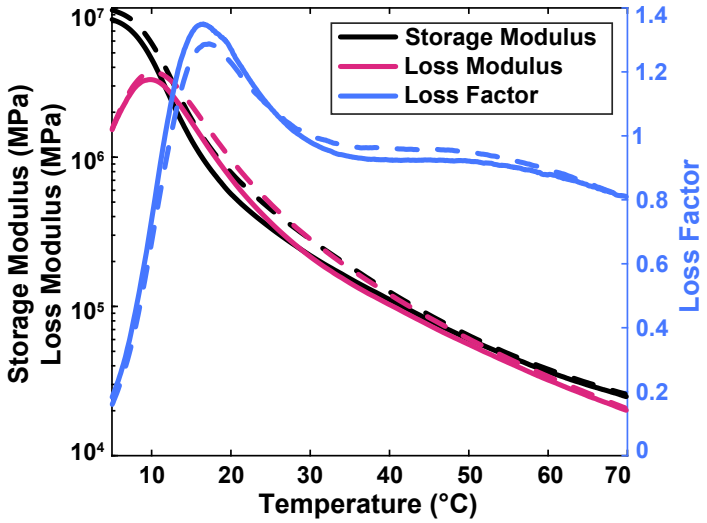


**Supporting Figure S13:** Rheological analysis of two cast specimens (solid and dashed lines) loaded in torsion under continuous temperature sweeps.

The glass transition temperature of the material is approximately 10 °C as calculated from the maxima of the loss modulus per ASTM D4065.

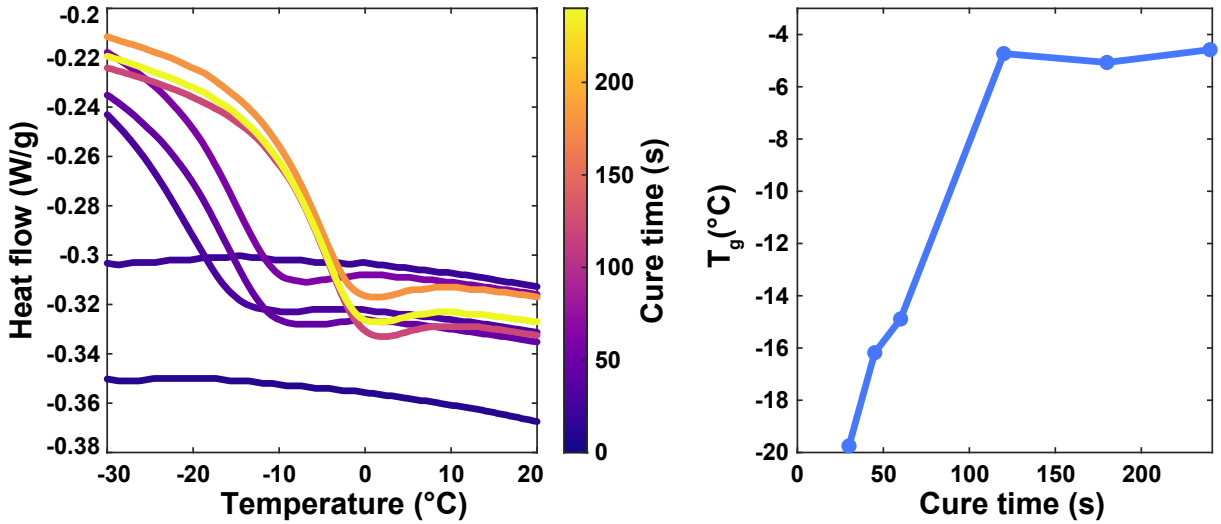


**Supporting Figure S14:** Differential scanning calorimetry of curing resin.

DSC thermograms (5 °C/min, N2 atmosphere) were obtained using a TA Instruments Discovery 2500 DSC from samples irradiated (365 nm, 2.9 mW/cm$^2$) for 0, 10, 20, 30, 45, 60, 120, 180, and 240 s and stored under ambient conditions for less than 24 hr, and used to track the evolution of the glass transition temperature ($T_g$) as a function of the total irradiation time. A noticeable $T_g$ at -20 °C can be observed after irradiation for 30 s, indicating that a significant amount of monomer has been converted into polymer. The $T_g$ continues to increase in temperature as the irradiation time is extended, eventually plateauing at -5 °C after 120 s of total irradiation time. This suggests that the resin continues to cure after 30 s, and is fully cured between 60-120 s of total irradiation time.

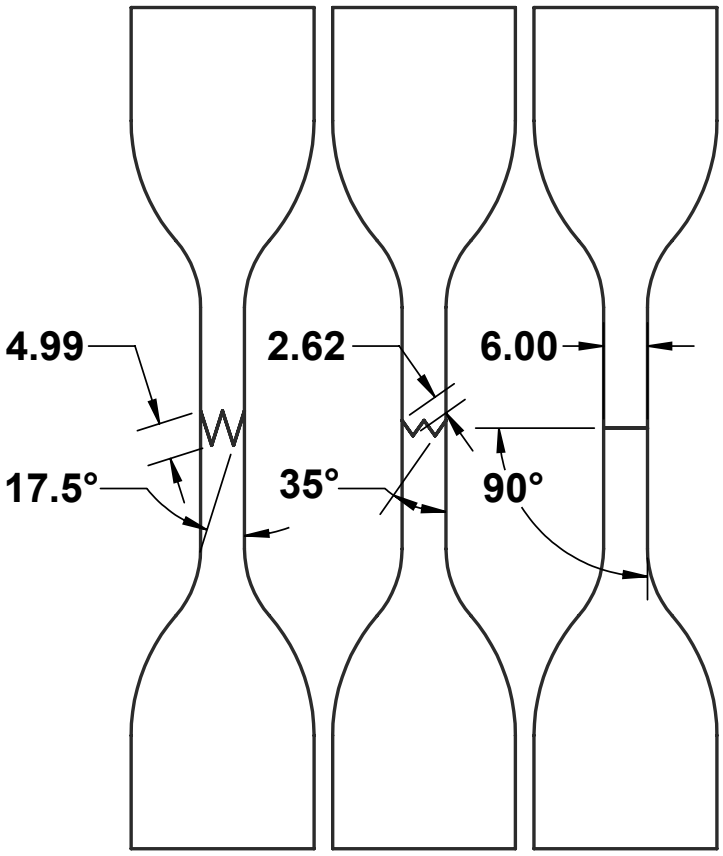


**Supporting Figure S15:** Design drawing with dimensions (mm) of the modified ASTM D412 type C tensile specimens used to study the effect of self-healing interfaces.

To study the role of interfacial geometry on self-healing, three modular specimens were designed. Two specimens had herringbone geometries at the interface. The flat interface geometry was used as a control. The specimen geometries adhere to the ASTM D412 test standard. All measurements are in mm.

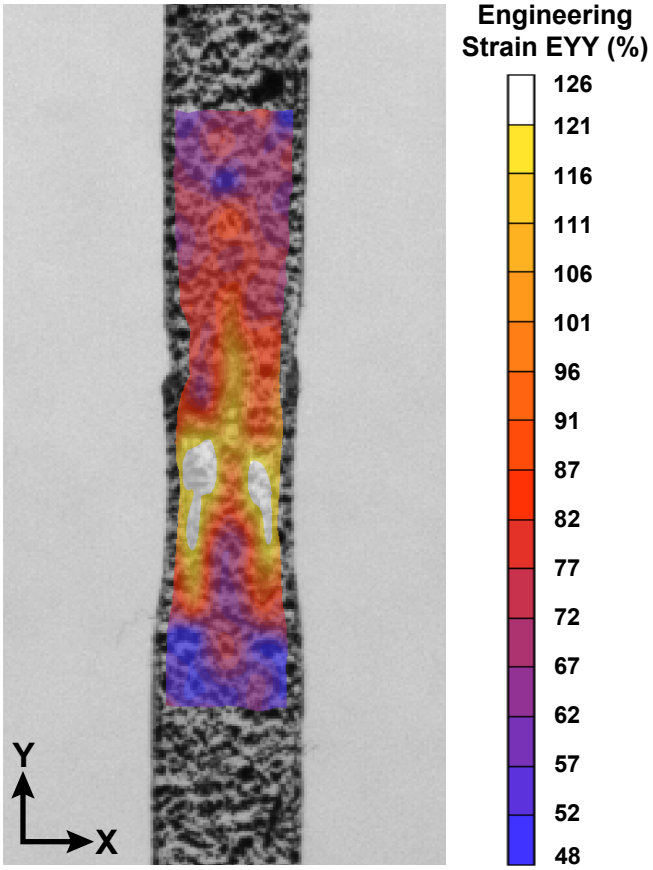


**Supporting Figure S16:** DIC measurements of a cast 17.5° herringbone grafted specimen showing strain localization near the interface.

Local strain measurements calculated using 2D DIC were used to study strain inhomogeneities near the grafted surface. Axial strain measurements reveal prominent strain localizations near the 17.5° herringbone interface forming during early stages of the test.

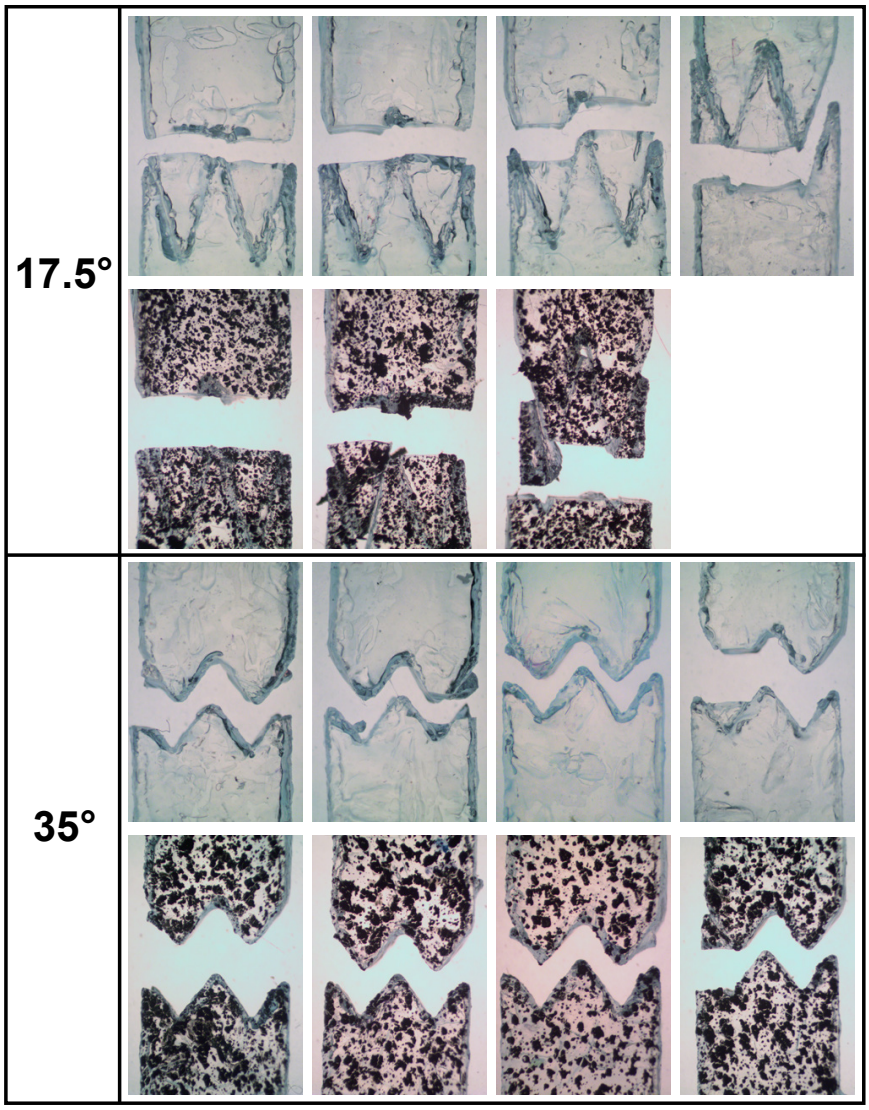


**Supporting Figure S17:** Bright-field microscope images of 17.5° (top) and 35° (bottom) herringbone grafted specimens after fracture under uniaxial tension.

After the grafted samples were fractured, bright-field microscope images were taken of each sample's fracture interface. The results demonstrate repeatable fracture behavior among samples. All of the 17.5° samples fractured across the center of the sample, fracturing the herringbone teeth in the process. The 35° samples generally only split the outermost teeth of the graft. This study suggests that a spectrum of fracture behaviors and mechanical properties are achievable using different pattern angles.

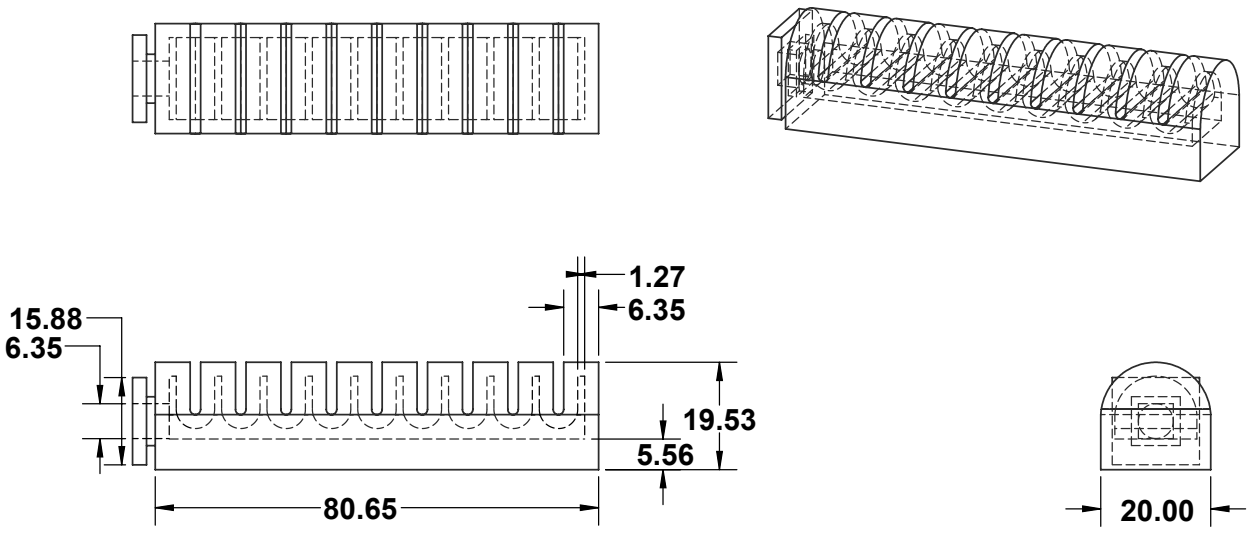


**Supporting Figure S18:** Design drawing with dimensions (mm) of the pneumatic actuator and gasket used in the autonomous self-healing experiment.

To validate the rapid functionality restoration enabled by the material, a generic soft robotic actuator was designed and DLP printed without internal supports. The final weight of each printed actuator was approximately 29.66 g after post-curing and desiccator storage. All walls were sized to keep undesired bulging of the individual bellows to a minimum while maintaining good actuation. The robot was mounted to a pneumatic line using a gasket. All dimensions are in mm.

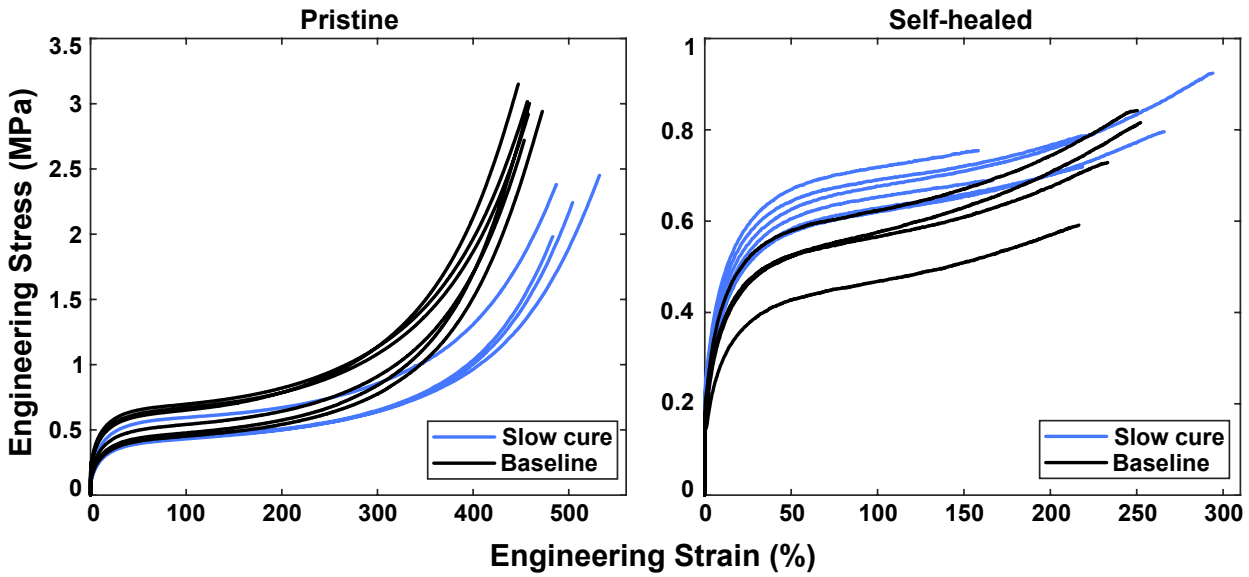


**Supporting Figure S19:** Equivalence of curing techniques for cast specimens using uniaxial tension testing.

In some later tests in this work the curing was partitioned into several shorter cures to slow the polymerization and thus discourage defect formation (e.g., voids). The baseline cure used in a majority of this work was a 4 min cure at a 25 cm stand-off distance and 25% intensity on the UV light source. The slowed curing regimen maintained the same stand-off distance and intensity. The new curing method used three cure-rest cycles (10-s cure/1-min rest), followed by a 4 min continuous cure. The incremental curing approach slowed the polymerization process in order to lower peak temperatures during curing (measured at $>$100 °C with the original curing method), reducing the number of samples with bubbles that needed to be discarded. The near mechanical equivalence of specimens cured using these two approaches (continuous vs. incremental polymerization) was demonstrated.

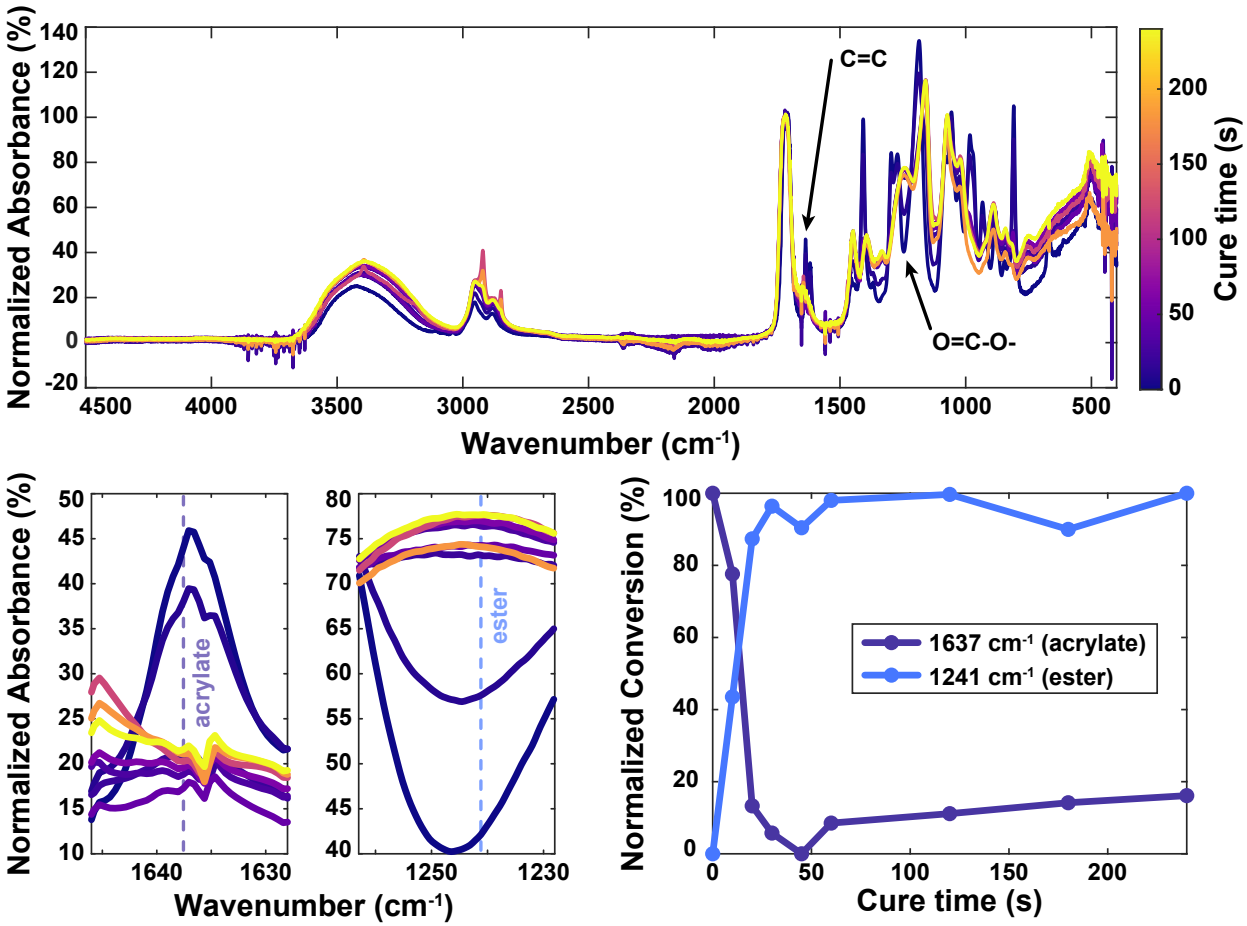


**Supporting Figure S20:** Fourier transform infrared spectroscopy of curing resin.

ATR-FTIR spectra were obtained from samples after irradiation (365 nm, 2.9 mW/cm$^2$) for 0, 10, 20, 30, 45, 60, 120, 180, and 240 s. Tests were conducted on a Bruker Alpha-P FTIR spectrophotometer equipped with an attenuated total reflectance attachment. All spectra were normalized based on their intensities at 1721 cm$^{-1}$, which allowed for monitoring of the alkene and ester peaks at 1637 and 1241 cm$^{-1}$, respectively, as a function of increasing irradiation time. The bottom left shows an inset depicting normalized absorbance of the acrylate alkene stretch at 1637 cm$^{-1}$, demonstrating a reduction in absorption of the alkene as irradiation time increases. The bottom middle graph depicts an inset showing the normalized absorbance of the ester stretch at 1241 cm$^{-1}$, demonstrating an increase in the absorption of the ester with increasing irradiation time. The bottom right graph plots the normalized conversion of the alkene and ester as a function of cure time. From this data, we observe that the conversion of the alkene from the monomer appears to plateau between 30 and 60 s of irradiation time at 365 nm. Attempts were also made to track conversion of the thiol; however, the S-H stretches that occur at 2558 cm$^{-1}$ are typically weak, and due to the low concentration of the thiol in our formulation, we were not able to meaningfully detect the presence or conversion of thiol.

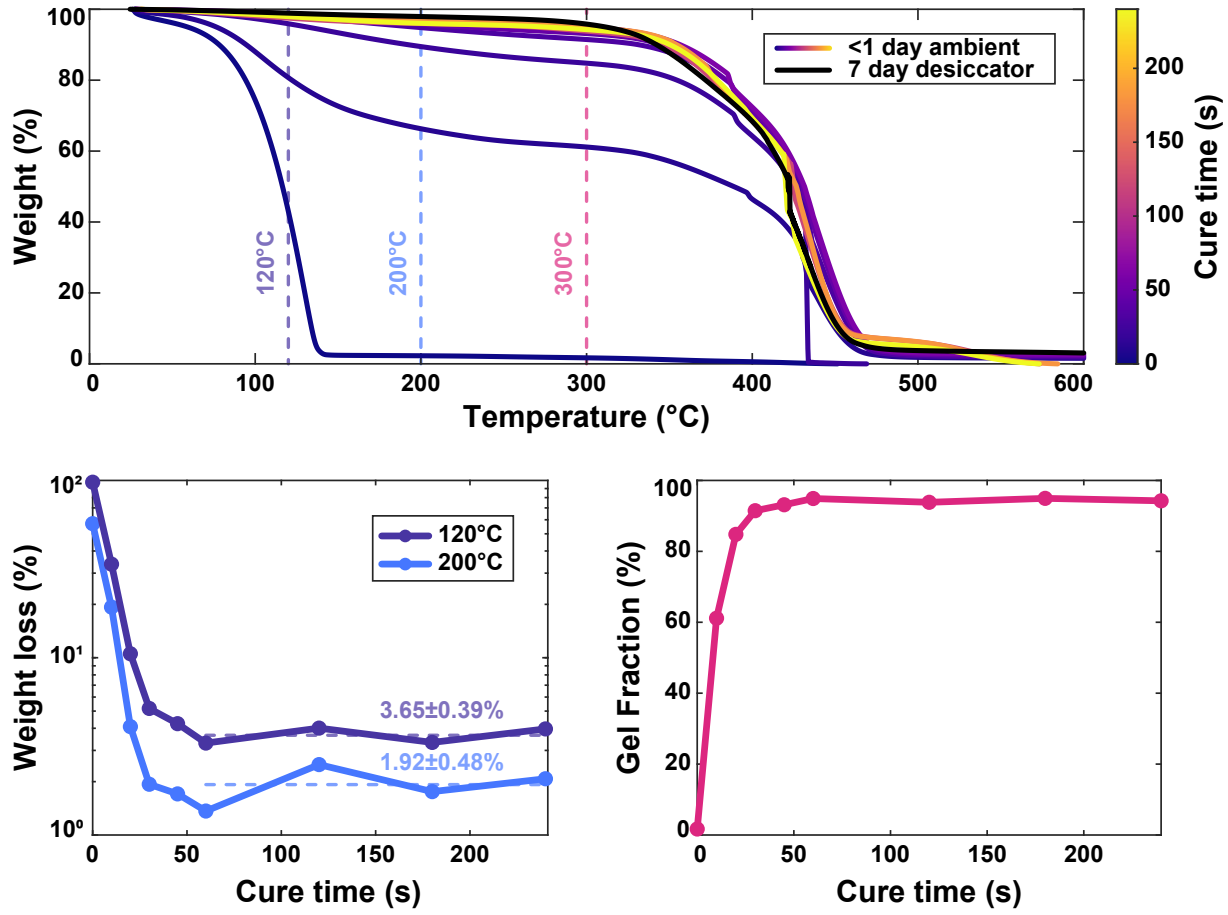


**Supporting Figure S21:** Thermal gravimetric analysis (TGA) of curing resin.

TGA thermograms (10 °C/min, nitrogen atmosphere) were obtained using a TGA (5500, TA Instruments, New Castle, DE, USA) from samples irradiated (365 nm, 2.9 mW/cm$^2$) for 0, 10, 20, 30, 45, 60, 120, 180, and 240 s and stored under ambient conditions for less than 24 hr. This is compared to a 240 s cured sample stored in a desiccator for seven days. The bottom left graph plots the weight loss at 120 °C and 200 °C, corresponding to estimated losses of water and both water and uncured monomer, respectively, as a function of total irradiation time. The bottom right graph plots the gel fraction (taken as the mass remaining at 300 °C) as a function of total irradiation time. This data demonstrates that the gel fraction has mostly reached a maximum by 30 s of irradiance.

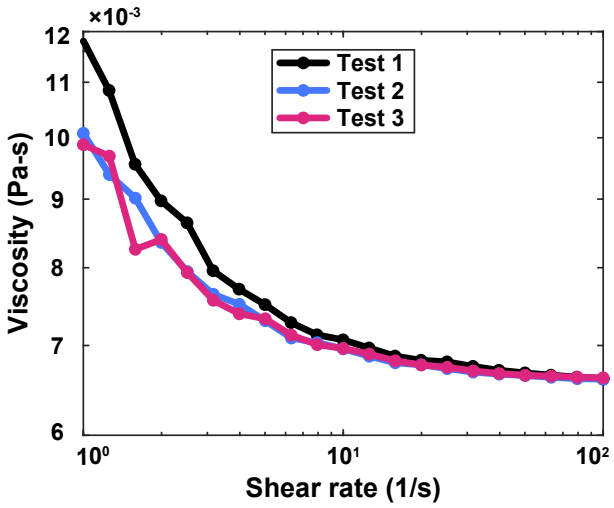


**Supporting Figure S22:** Rheological analysis of the uncured resin over a range of shear rates.

The low viscosity of resin contributes to its compatibility with vat photopolymerization 3D printing. To quantify the resin's resistance to flow, rheological testing was conducted. Results indicate shear thinning, with the viscosity settling to about 0.007 Pa-s at higher shear rates. This is driven primarily by the low viscosity of HEA, which composes a majority of the resin.

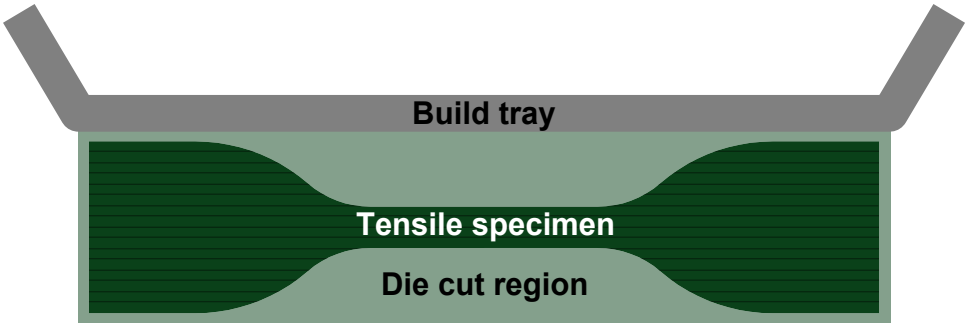


**Supporting Figure S23:** Build tray orientation of DLP tensile specimens (layer thickness not drawn to scale).

To study material strength, rather than interlayer adhesion, specimens were intentionally printed with layer faces oriented orthogonal to the applied load in uniaixal tension tests.

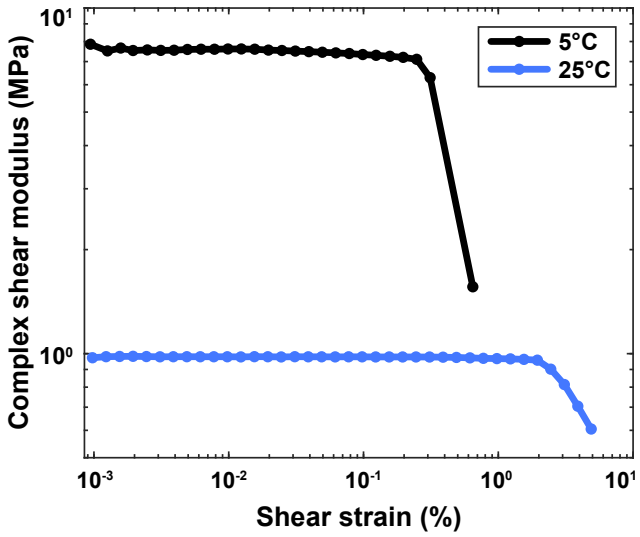


**Supporting Figure S24:** Rheological analysis examining the variation of complex modulus with shear strain in cast specimens.

In order to bound the linear viscoelastic region of the material's torsional response, shear strain amplitude sweeps were performed at 5 °C and 25 °C. As expected, at 5 °C, the material exhibits stiffer response and a narrower band of linear elastic response. At room temperature (25 °C), the response transitions from linear viscoelastic to nonlinear viscoelastic around $2\%$ strain. Subsequent dynamic mechanical analyses (Figs. S12-13) were performed under angle control up to a maximum strain of $0.00625\%$ (torsional angle of 10 $\mu$rad), significantly below the material's linear-to-nonlinear transition.